Radio Science®

RESEARCH ARTICLE
10.1029/2025RS008508

Special Collection:
Future Opportunities in Deep Space Communications and Navigation

On the Electromagnetic Energy Flow Along Geodesics

Jacob T. Fokkema[1] and **Peter M. van den Berg**[1]

[1]Delft University of Technology, Delft, The Netherlands

Abstract We present a field-theoretic framework for modeling electromagnetic energy propagation in heterogeneous media by introducing the concept of electromagnetic geodesics. Unlike traditional ray optics, which assumes either a straight-line propagation or a simple bending in refractive media, our approach formulates wave propagation as geodetic motion in a curved spatial geometry induced by variations in refractive index. Building on earlier work, we move beyond scalar refractive index analogies and instead construct a local Riemannian metric characterized by an orthogonal geometric tensor derived from the Helmholtz representation. This tensor encodes spatial anisotropy and curvature, enabling a rigorous description of energy flow through complex media. We derive the electromagnetic geodesics by formulating and solving a Lagrangian system, yielding equations of motion for wavefront trajectories, group velocity, and intensity distribution. The concept of refractive tension—the vector displacement between Euclidean and transformed positions—plays a central role in defining the transformation matrix and associated metric. Numerical simulations for a spherical inhomogeneity embedded in vacuum demonstrate the emergence of curved geodesics and localized energy redistribution, illustrating the model's potential for interpreting interstellar electromagnetic phenomena and refractive effects in astrophysical environments. In particular, it shows the spatial dispersion of a the energy flow in the vicinity of the spherical inhomogeneity.

Plain Language Summary We propose a new way to describe how light and electromagnetic energy move through complex materials. Instead of straight or bent paths, waves follow curved "geodesics" shaped by refractive index changes. This geometric approach explains energy flow, predicts intensity patterns, and helps interpret astrophysical and interstellar phenomena.

Key Points:

- Geodesic-Based Framework for Electromagnetic Propagation
- Wavefronts and Energy Flow of Harmonic waves
- Emergent Wave Effects Beyond Classical Optics

Correspondence to:
J. T. Fokkema,
j.t.fokkema@tudelft.nl

Citation:
Fokkema, J. T., & van den Berg, P. M. (2026). On the electromagnetic energy flow along geodesics. *Radio Science*, *61*, e2025RS008508. https://doi.org/10.1029/2025RS008508

Received 2 OCT 2025
Accepted 2 JAN 2026

1. Introduction

In our paper, Fokkema and Van den Berg (2020), we explored a novel conceptual framework for understanding the propagation of electromagnetic energy. Traditionally, electromagnetic waves are often analyzed using ray optics, where it is assumed that rays travel either in straight lines in homogeneous media or bend predictably in media with local variations of the refractive index. However, this simplification fails to capture the complexities encountered in heterogeneous environments, such as those found in interstellar space. To address this, we proposed a shift from the traditional concept of ray paths to that of geodetic paths in which electromagnetic energy follows in a curved space defined by variations in refractive index. This approach is rooted in the understanding that the transmission of electromagnetic energy is best described by the geodetic path, a trajectory dictated by the underlying geometry of the medium. We conducted a detailed 3D simulation of electromagnetic fields interacting with a spherical object possessing a contrasting refractive index. Our wave-front analysis revealed that, as the electromagnetic waves propagate, they do not follow simple straight lines. Instead, they adhere to geodesics, which are influenced by the global spatial variations in the refractive index. When passing close to the object, these geodesics exhibit noticeable deflections, an emergent property resulting from the interaction with the interior medium of the object. Unlike traditional rays, geodesics incorporate information about the curvature of space induced by the medium's refractive properties, making them particularly suitable for detailed interstellar observations. This capability to encode information about the objects they pass can potentially enhance our understanding of complex astrophysical phenomena, see Benningfield (2020).

Our approach diverges from existing methods that introduce a non-uniform refractive index in vacuum to model gravitational lensing, which draw analogies between gravitational and conventional optical lensing within the framework of general relativity. For instance, Ye and Lin (2007) derived an inhomogeneous vacuum refractive index in the Schwarzschild metric via Fermat's principle in general relativity. In the weak-field limit, this index assumes an exponential dependence on the gravitational potential, enabling calculations of light deflection, time delays, and image formation within an optical framework. Nazeri and Nouri-Zonoz (2011) argued, based on the

behavior of Casimir vacuum energy in a gravitational field, that the vacuum itself acts as a refractive medium, thereby linking space-time curvature directly to variations in the refractive index. Chyla (2012) addressed frequency-dependent effects by analyzing broadband spectral intensity to examine the interplay between achromatic gravitational lensing and chromatic electromagnetic phenomena. More recently, Yun and Jang (2022) proposed a hybrid model that computes light deflection by integrating gravitational fields with reflectivity-based physics via a generalized Snell's law, bridging classical optics and relativistic metrics.

In contrast, our method does not rely on imposing an effective refractive index to mimic general relativistic effects through an optical analogy. Rather, it emerges from a field-theoretical framework; to be specific the electromagnetic framework. The foundation of this new perspective lies in the local metric of the spatial wave phenomenon, characterized by a geometric tensor. We demonstrated, using the Helmholtz representation theorem, that this tensor is directly related to the contrast in the refractive index of the object. We showed that this geometric tensor is orthogonal, simplifying the mathematical treatment of the problem. Therefore, in our present paper, we analyze the geometric tensor in a local curved space with orthogonal bases in a Riemannian geometry. This implies that we now assume that the geodetic tensor in a local domain is diagonal. Note that in our previous paper, the effective refraction index along the geodesic is a scalar quantity that depends not only on the position, but also on the direction of the geodesic, which means that the diagonal terms are the same. To improve this scalar model, we consider a diagonal tensor with different terms. This paper develops the general formulation of the electromagnetic geodesic.

In Section 2, we begin with the concept of *optical length* and transition from a geometric optics framework, where time is the scaled quantity, to a geodesic description in which space itself is scaled. This transition necessitates a linear transformation from the original Euclidean space into a corresponding Riemannian space, laying the foundation for the geometric reinterpretation of light propagation.

In Sections 3 and 4, we introduce the geodesic by defining its line element and the transformation matrix that facilitates the spatial mapping. The matrix is constructed based on a quantity we denote as *refractional tension*, which is represented by the difference vector between the original position vector and its image in the transformed Riemannian space. This development naturally leads to the concept of the geodesic.

In Section 5, we define the *fundamental orthogonal geometric tensor*. This tensor encapsulates the essential geometric structure required to formulate the light trajectory in curved space. With these core ingredients established, we construct the geodesic explicitly. We formulate the Lagrangian governing the system and, by applying the Euler-Lagrange equations, we derive the equations of motion that describe the geodesic path.

In Section 6, we investigate how the refractional tension is related to the inhomogeneous distribution of the refractive index of a finite object inside a simply closed domain embedded in vacuum. We achieve a practical and computationally tractable framework for the determination of the refractional tension. This enables a broader application of the theory for arbitrary geometries. Further we incorporate the concept of group velocity to analyze the variation of light intensity along the geodesic. Here, we encounter a dynamic interplay between kinetic and potential energy, a form of energy exchange governed by the underlying physical context. Notably, the total energy is not conserved; rather, it is the difference between kinetic and potential energy that plays a crucial role. Building on the symmetry of a radially symmetric object, a homogeneous sphere is used as a specific case study, demonstrating the application of the developed formalism in a physically relevant scenario. In particular, it is illustrated how a harmonic wave propagates along a geodesic; it loses its energy after bending toward the sphere and recovering this energy propagating away from the sphere. Finally, we present and discuss numerical results obtained from simulating the spherical case, offering insights into the physical implications and validating the theoretical framework.

In Section 7, we present two applications for practical use of geodesics. The first arises from astrophysics, where the Shapiro two-way time is used to characterize the geometrical tensor of interstellar objects and to probe the electromagnetic properties of the Corona around the Sun. The second application is found in optics, where we study the focusing effects of the Lüneburg lens.

In Sections 8 and 9, we conclude the study by summarizing the key theoretical advancements and highlighting the potential applications.

2. Geometrical Optics

In geometrical optics, the propagation of electromagnetic energy density along a certain ray path in the original frame is studied in a Cartesian space with position vector $\boldsymbol{x} = \{x^1, x^2, x^3\}$. We first follow the classical formulation of light rays of Born and Wolf (1959).

The optical length ds is defined as the product of the vacuum velocity of light and the time dt needed for light to propagate along the line element ds, viz.,

$$\mathrm{d}s = c_0\,\mathrm{d}t, \quad \text{with} \quad \mathrm{d}t = \mathrm{d}l/c, \tag{1}$$

in which $c = c(\boldsymbol{x})$ is the velocity of light in an inhomogeneous medium. Note that when $c = c_0$, then $\mathrm{d}l = \mathrm{d}s$. Further, we write

$$\mathrm{d}s = n(\boldsymbol{x})\,\mathrm{d}l, \quad \text{with} \quad n(\boldsymbol{x}) = c_0/c(\boldsymbol{x}), \tag{2}$$

where n is the spatially dependent refractive index. Then (Equation 2) is written as

$$\mathrm{d}s = n\sqrt{(\mathrm{d}x^1)^2 + (\mathrm{d}x^2)^2 + (\mathrm{d}x^3)^2}. \tag{3}$$

In the optical description, (Equation 3) leads to the *eikonal equation* given by

$$n^2\left[\left(s^1\right)^2 + \left(s^2\right)^2 + \left(s^3\right)^2\right] = 1, \quad \text{with} \quad s^i = \mathrm{d}x^i/\mathrm{d}s, \quad \text{for } i = 1,2,3. \tag{4}$$

The differential equation for the optical path (ray) is given by, see p. 122 of Born and Wolf (1959),

$$\mathrm{d}\left(n\,s^i\right)/\mathrm{d}s = \mathrm{d}n/\mathrm{d}x^i. \tag{5}$$

In a previous paper, Fokkema and Van den Berg (2019), we introduced a modification of the ray theory by assuming that under influence of a refractional tension, the refractive index becomes also dependent on the direction vector s^i, hence $n = n\left(\boldsymbol{x}, s^i(\boldsymbol{x})\right)$. In each point $\boldsymbol{x}$ of the iterative Euler solution of (Equation 3), we rotate the local coordinate system to determine the new direction vector and the propagation path. Although this method improves the insight of wave propagation passing a refractive object substantially, it is in principle a small-curvature approximation of the path. This restricts the value of the refractive index. To relax this limitation, we consider a Riemannian space in which there exists a linear relation between the original Cartesian frame $\boldsymbol{x} = \{x^1, x^2, x^3\}$ and the transformed frame $\bar{\boldsymbol{x}} = \{\bar{x}^1, \bar{x}^2, \bar{x}^3\}$, see for example, Synge and Schild (1978), p. 28. The optical length of (Equation 3) can be rewritten as

$$\mathrm{d}s = \sqrt{\left(\mathrm{d}\bar{x}^2\right)^2 + \left(\mathrm{d}\bar{x}^2\right)^2 + \left(\mathrm{d}\bar{x}^3\right)^2}, \quad \text{with } \mathrm{d}\bar{x}^i/\mathrm{d}x^i = n(\boldsymbol{x}), \quad \text{for } i = 1,2,3. \tag{6}$$

We observe that the optical length ds also can be written as a change in the geometrical description. Thus instead of changing the local wave velocity, space has to be adapted to arrive at the same optical length. The formulation of (Equation 6) hints to the introduction of the geometrical tensor that determines space depending on the variation of the refractive index in the medium. This formulation introduces a *global dependency*, in contrast to classical geometric optics, which is governed solely by *local* variations. In geometric optics, the system is sensitive only to changes occurring at a point or infinitesimally nearby. However, in the present case, spatial transformations are influenced by broader structural properties of the surrounding space. We observe a fundamental distinction: in the optical framework, it is *time* that undergoes scaling, while in our geometric framework, it is *space* that is subject to transformation. This shift in perspective has significant implications for the representation and interpretation of the transformation tensor. Specifically, representation (Equation 5) takes the form of an *orthogonal transformation* in which all spatial axes are uniformly scaled down by a factor of n, the refractive index. The trace of the tensor that plays a fundamental role in this transformation is given by

$$\nabla \cdot \bar{\boldsymbol{x}} = \sum_{i=1}^{3} \mathrm{d}\bar{x}^i / \mathrm{d}x^i = 3\,n, \tag{7}$$

reflecting uniform scaling across the three orthogonal directions of our three-dimensional space. It is important to note that the factor of 3 arises directly from the dimensionality of the ambient space. More critically, the trace of the transformation tensor constitutes a *principal invariant*, a scalar quantity that remains unchanged under orthogonal transformations, including rotations of the coordinate system. This makes the trace an objective quantity, satisfying the *principle of material frame-indifference*. As stated by Šilhavý (1997), frame-indifference requires that physical laws remain valid and form-invariant under any change of observer, specifically under rotations and translations of the frame. In the subsequent analysis, we adopt this frame-indifferent perspective by maintaining the scaling relation governed by the refractive index n. To preserve consistency with physical laws, we enforce the local invariance of the trace-ensuring that under any permissible local rotation, the trace of the transformation tensor remains constant.

3. Line Element in Riemannian Space

In geometrical optics, we have shown that the distortion of the spatial framework $\bar{\boldsymbol{x}}$, or in other words the divergence of $\bar{\boldsymbol{x}}$, is related to the refractive index: see (Equation 6) and (Equation 7). We generalize the distance norm in the transformed space as

$$\mathrm{d}s^2 = g_{ij}\mathrm{d}\bar{x}^i\mathrm{d}\bar{x}^j, \quad \text{with } g_{ij} = \frac{\partial x^k \partial x^k}{\mathrm{d}\bar{x}^i \mathrm{d}\bar{x}^j}, \tag{8}$$

where we have used Einstein's summation convention for repeated indices. The tensor g_{ij} is the metric tensor of the spatial transformation and in view of its symmetry this tensor can be diagonalized. After diagonalization, the distance norm is written as

$$\mathrm{d}s^2 = g_{11}\left(\mathrm{d}\bar{x}^1\right)^2 + g_{22}\left(\mathrm{d}\bar{x}^2\right)^2 + g_{33}\left(\mathrm{d}\bar{x}^3\right)^2. \tag{9}$$

In fact, the coordinates of $\bar{\boldsymbol{x}}$ represent the actual coordinates of our local transformed frame at each point $\boldsymbol{x}$. To progress toward an operational expression for the transformation tensor, we now introduce the concept of the *difference vector*, defined between two spatial points. This vector captures the displacement between a position in the original (Euclidean) configuration and its corresponding image in the transformed (Riemannian) configuration, and serves as the foundation for constructing a concrete form of the transformation. We introduce the difference vector between the points $\bar{x}^k$ and x^k as

$$f^k = \bar{x}^k(\boldsymbol{x}) - x^k, \tag{10}$$

in which f^k is a continuous and differentiable vector field. Next taking the divergence of f^k and using (Equation 7), we obtain

$$\mathrm{div}\,\mathbf{f} = \partial f^k / \partial x^k = \partial \bar{x}^k / \partial x^k - 3 = 3[n(\boldsymbol{x}) - 1]. \tag{11}$$

Here, $3[n(\boldsymbol{x}) - 1]$ can be interpreted as a contrast source in a vacuum embedding with refractive index $n = 1$ and $\mathrm{div}\,\mathbf{f} = 0$. We assume that in this vacuum embedding, the tension $\mathbf{f}$ is a conservative vector field following from a scalar potential Φ with the properties that

$$\mathbf{f} = -\mathrm{grad}\,\Phi, \quad \mathrm{curl}\,\mathbf{f} = \mathbf{0}, \quad \text{and} \quad \mathrm{div}\,\mathbf{f} = -\mathrm{div}\,\mathrm{grad}\,\Phi. \tag{12}$$

This potential field is the supporting framework for the determination of the geodetic paths, on which the electromagnetic wave field experiences the least-action from this refractional tension. This framework is denoted as the Riemannian space. Before we discuss the trajectory of the geodesics, we make some observations. In view

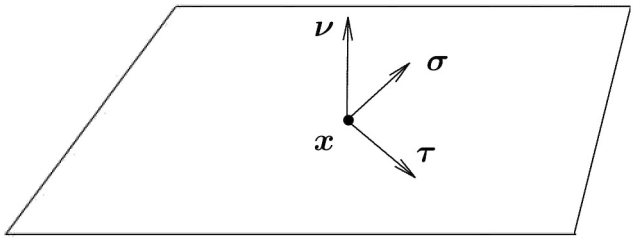

Figure 1. The tangential plane in a point $\boldsymbol{x}$ spanned by the unit vectors $\boldsymbol{\tau}$ and $\boldsymbol{\sigma}$. The unit vector $\boldsymbol{\nu}$ is the normal to the local infinitesimal flat surface Φ = constant.

of vanishing curl of the tension, it follows from Kelvin-Stokes theorem that for any closed path the net circulation integral of the tension vector $\mathbf{f}$ over some closed curve is zero. Let the net circulation integral over a path between two positions $\boldsymbol{x}_A$ and $\boldsymbol{x}_B$ be defined as

$$\int_{\boldsymbol{x}_A}^{\boldsymbol{x}_B} \boldsymbol{f} \cdot \mathrm{d}\boldsymbol{s} = \Phi(\boldsymbol{x}_A) - \Phi(\boldsymbol{x}_B), \tag{13}$$

in which $\boldsymbol{s}$ is the direction vector along the path. For the actual geodesic based on Hamilton's principle of least action between these two points we now conclude that the net action in the tangential direction of the geodesic is constant, for all curves between these two fixed points. It is the contribution of the action in the normal direction to the geodesic that determines the curvature.

4. Transformation Matrix in Cartesian Space

The transformation matrix is defined as

$$C_{ij}(\boldsymbol{x}) = \partial \overline{\boldsymbol{x}}^i / \partial \boldsymbol{x}^j = \delta_{ij} + \partial_i f_j, \tag{14}$$

where we have used the spatial derivative of (Equation 10) with respect to x^i and $\partial_i = \partial/\partial x^i$. Note that in our analysis C_{ij} is a tensor of second order, but for the determination of the eigenvalues we use the matrix representation. Using $f_j = -\partial_j \Phi$, we write the transformation matrix as $C_{ij} = \delta_{ij} - \partial_i \partial_j \Phi$. Since the matrix C_{ij} is real and symmetric, an eigenvalue decomposition with positive eigenvalues exists and the sum of the eigenvalues is equal to the trace. By inspection of (Equation 14), we learn that in the transform geometry the coordinate axes are spanned by the components of the tension $\mathbf{f}$. In our physical model it is always possible to define surfaces with constant potential Φ. In view of $f_j = -\partial_j \Phi$, the tension is directed in the normal direction to the surface Φ = constant. At a point $\boldsymbol{x}$, see Figure 1, where the geodesic crosses such a surface, we define the vector $\boldsymbol{s}$ in the direction of evolution of the geodesic. Further we define a local plane tangent to the curved surface Φ = constant, with unit normal vector $\boldsymbol{\nu}$ and unit tangent vector $\boldsymbol{\tau}$ and unit bi-tangent vector $\boldsymbol{\sigma}$. These three vectors form the basis of a local orthonormal right-handed coordinate system. Note that at this point the tangential directions $f_\tau = -\partial_\tau \Phi$ and $f_\sigma = -\partial_\sigma \Phi$ vanish, because Φ = constant at the point $\boldsymbol{x}$.

The normal vector $\boldsymbol{\nu}$ is related to the tension vector as $\nu_i = f_i/f$ where $f = |\boldsymbol{f}|$. We consider it to be an eigenvector $\lambda^{(\nu)}$ belonging to the matrix C_{ij}. To indicate that the eigenvalue is a scalar quantity, we use parentheses in the superscript. The eigenvalue $\lambda^{(\nu)}$ follows from $C_{ij}\nu_j = \lambda^{(\nu)}\nu_i$. Multiplying both sides by ν_i, we obtain

$$\lambda^{(\nu)} = 1 - \nu_i \nu_j \partial_i \partial_j \Phi, \tag{15}$$

which shows that this eigenvalue is obtained from the matrix C_{ij} by contraction with the vectors ν_i and ν_j. We observe that (Equation 15) can be written in terms of the scalar value f. From $f^2 = f_i f_i$ it follows that $f_j \partial_i f_j = f \partial_i f$, and using $f_j = -\partial_j \Phi$ we arrive at

$$\lambda^{(\nu)} = 1 + \mathcal{D}_\nu f, \tag{16}$$

where $\mathcal{D}_\nu = \nu_i \partial_i$ is known as the directional derivative in the direction of $\boldsymbol{\nu}$. This eigenvector is complemented with the other eigenvectors $\boldsymbol{\tau}$ and $\boldsymbol{\sigma}$ with corresponding eigenvalues $\lambda^{(\tau)}$ and $\lambda^{(\sigma)}$. Since C_{ij} is real and symmetric we also know that, for distinct eigenvalues, the eigenvectors are orthogonal. Since the trace of a symmetric operator is equal to the sum of the eigenvalues, it follows from (Equation 7) that $\lambda^{(\nu)} + \lambda^{(\tau)} + \lambda^{(\sigma)} = 3n$. The eigenvalues $\lambda^{(\tau)}$ and $\lambda^{(\sigma)}$ for the tangential eigenvectors are identical. They are then obtained as

$$\lambda^{(\tau)} = \lambda^{(\sigma)} = \frac{1}{2}(3n - 1) - \frac{1}{2}\mathcal{D}_\nu f. \tag{17}$$

If two of the three eigenvalues are the same, Dietrich (2016) has shown that, in the plane perpendicular to the principal eigenvector $\boldsymbol{\nu}$, the orientation of the eigenvectors belonging to these repeated eigenvalues may be chosen arbitrarily. Hence, we select an orthogonal basis in the Riemannian space $\bar{\boldsymbol{x}} = \{x^\nu, x^\tau, x^\sigma\}$ with the eigenvalues $\{\lambda^{(\nu)}, \lambda^{(\tau)}, \lambda^{(\sigma)}\}$.

5. Geodesics

We now return to the line element ds and we select an orthonormal basis in the Riemannian space $\bar{\boldsymbol{x}} = \{x^\nu, x^\tau, x^\sigma\}$ with unit vectors $\boldsymbol{\nu}$, $\boldsymbol{\tau}$ and $\boldsymbol{\sigma}$. The eigenvalue decomposition defines the arc length in the transformed frame, viz.,

$$\mathrm{d}s^2 = g_{\nu\nu}\,(\mathrm{d}x^\nu)^2 + g_{\tau\tau}\,(\mathrm{d}x^\tau)^2 + g_{\sigma\sigma}\,(\mathrm{d}x^\sigma)^2, \tag{18}$$

where g is the covariant metric tensor with components

$$g_{\nu\nu} = 1/\big(\lambda^{(\nu)}\big)^2, \quad g_{\tau\tau} = 1/\big(\lambda^{(\tau)}\big)^2, \quad g_{\sigma\sigma} = 1/\big(\lambda^{(\sigma)}\big)^2. \tag{19}$$

Since $\lambda^{(\tau)} = \lambda^{(\sigma)}$ we note that $g_{\tau\tau} = g_{\sigma\sigma}$. The relations (Equation 18) for the line element ds and (Equation 19) for the metric tensor form the fundamental basis to construct the geodetic path, defined as the geodesic, see Synge and Schild (1978) and de Souza Sánchez Filho (2015). Note that dividing (Equation 18) by ds^2 results into

$$g_{\nu\nu}(s^\nu)^2 + g_{\tau\tau}(s^\tau)^2 + g_{\sigma\sigma}^2(s^\sigma)^2 = 1, \text{ with } s^\nu = \mathrm{d}\bar{x}^\nu/\mathrm{d}s,\ s^\tau = \mathrm{d}\bar{x}^\tau/\mathrm{d}s,\ s^\sigma = \mathrm{d}\bar{x}^\sigma/\mathrm{d}s, \tag{20}$$

where $\boldsymbol{s}$ is an unit vector in the Riemannian space with property $s_\nu s^\nu + s_\tau s^\tau + s_\sigma s^\sigma = 1$. In fact, this equation is the counterpart of the *eikonal equation* in optics, see (Equation 4). The metric tensor can be used to lower the index of a contravariant vector to get a covariant vector, for example $s_\nu = g_{\nu\nu}s^\nu$, if necessary. Further, often we raise the indices of a component of our diagonal tensor, for example $g^{\nu\nu} = 1/g_{\nu\nu}$. The curve in a Riemannian space which makes the distance a minimum is called a geodesic of that space. This curve follows from a variational procedure of the Lagrangian $\mathcal{L} = \sqrt{g_{ij}\,s^i s^j}$, with $s^k = \mathrm{d}\bar{x}^k/\mathrm{d}s$ and fixed begin point and end point. This leads to the Euler-Lagrange equations, see equation (2.114) of Synge and Schild (1978),

$$\frac{\mathrm{d}}{\mathrm{d}s}\frac{\partial \mathcal{L}}{\partial s^k} = \frac{\partial \mathcal{L}}{\partial \bar{x}^k}, \quad \text{or} \quad \frac{\mathrm{d}}{\mathrm{d}s}\left(\frac{1}{\mathcal{L}}\,g_{kj}\,s^j\right) = \frac{1}{2}\,\frac{1}{\mathcal{L}}\,s^i s^j\,\frac{\partial g_{ij}}{\partial \bar{x}^k}. \tag{21}$$

When the variational parameter is chosen equal to the arc length, see equation (2.416) of Synge and Schild (1978), and the second relation of (Equation 21) simplifies to

$$\frac{\mathrm{d}}{\mathrm{d}s}\big(g_{kj}s^j\big) = \frac{1}{2}\,s^i s^j\,\partial g_{ij}/\partial \bar{x}^k. \tag{22}$$

This leads to the well-known form of the geodesic equation with Christoffel symbols, see page 41 of Synge and Schild (1978). For our diagonal metric tensor in our local coordinates system, the Christoffel formulation is not needed. The Euler-Lagrange equations of (Equation 22) simplify substantially into

$$\frac{\mathrm{d}}{\mathrm{d}s}\big(g_{\nu\nu}\,s^\nu\big) = \frac{1}{2}\Big[(s^\nu)^2\,\partial_\nu g_{\nu\nu} + (s^\tau)^2\,\partial_\nu g_{\tau\tau} + (s^\sigma)^2\,\partial_\nu g_{\sigma\sigma}\Big], \tag{23}$$

with the conservative properties $\mathrm{d}\big(g_{\tau\tau}s^\tau\big)/\mathrm{d}s = 0$ and $\mathrm{d}\big(g_{\sigma\sigma}s^\sigma\big)/\mathrm{d}s = 0$, so that $g_{\tau\tau}\,s^\tau$ and $g_{\sigma\sigma}\,s^\sigma$ are constant along the geodesic. Further, we denote the location of the start point of the geodesic as $\boldsymbol{x}(0)$ and the unit direction vector as $\boldsymbol{s}(0)$. Then, for any point at the geodesic $\boldsymbol{x}$, the tangential components of the covariant direction vector $\boldsymbol{s}$ follow from the conservative properties as

$$\begin{cases} s_\tau = g_{\tau\tau}\, s^\tau(\boldsymbol{x}) = s^\tau(0) = s_\tau(0), \\ s_\sigma = g_{\sigma\sigma}\, s^\sigma(\boldsymbol{x}) = s^\sigma(0) = s_\sigma(0), \end{cases} \tag{24}$$

where $g_{\tau\tau}$ and $g_{\sigma\sigma}$ denote the tangential components of the geometric tensor at position $\boldsymbol{x}$. A fundamental result of the conservative properties is that the tangential directions of the contravariant direction vector are preserved. Along each geodesic, the covariant vectors s_τ and s_σ are constant. However, the contravariant vectors s^τ and s^σ are not constant. They are given by $s^\tau = g^{\tau\tau}(\boldsymbol{x})\, s_\tau$ and a similar relation for s^σ. We observe that $g_{\tau\tau}$ is equal to $g_{\sigma\sigma}$. Then, by selecting the initial value $s_\sigma = 0$ we have $g_{\sigma\sigma} = 0$, and without loss of generality we restrict the analysis to $g_{\tau\tau}$ only.

At this stage of our analysis we note that we have explicit expressions for the tangential component of the covariant direction vector along the geodesic in terms of the contravariant direction vector at its starting point. At a tangential plane where the tangential component of the metric vector is constant, the tangential derivative in the expression of

$$\mathrm{d}/\mathrm{d}s = s^\nu\, \partial/\partial x^\nu + s^\tau\, \partial/\partial x^\tau = s^\nu\, \partial/\partial x^\nu \tag{25}$$

vanishes. Since $\partial/\partial x^\nu$ is a derivative in a curved space, we use the concept of the physical component of the metric tensor, see Chapter V of Synge and Schild (1978), by including the factor $\sqrt{g^{\nu\nu}}$ in front of the normal derivative $\mathcal{D}_\nu$. We then have

$$\sqrt{g^{\nu\nu}}\, \partial g_{\nu\nu}/\partial x^\nu = \mathcal{D}_\nu g_{\nu\nu} \quad \text{and} \quad \sqrt{g^{\nu\nu}}\, \partial g_{\tau\tau}/\partial x^\nu = \mathcal{D}_\nu g_{\tau\tau}. \tag{26}$$

The relation between $g_{\nu\nu}$ and $g_{\tau\tau}$ follows directly from (Equation 20) as

$$g_{\nu\nu}(s^\nu)^2 + g_{\tau\tau}(s^\tau)^2 = 1, \qquad \text{with} \quad s^\nu = \mathrm{d}\bar{x}^\nu/\mathrm{d}s,\ s^\tau = \mathrm{d}\bar{x}^\tau/\mathrm{d}s. \tag{27}$$

The components of the direction vector are then obtained as

$$s^\tau = g^{\tau\tau} s_\tau, \quad s^\nu = \sqrt{g^{\nu\nu}}\sqrt{1 - g^{\tau\tau}(s_\tau)^2}. \tag{28}$$

We now return to (Equation 23). We apply the chain rule to its left-hand side, $\mathrm{d}\left(g_{\tau\tau}\, s^\nu\right)/\mathrm{d}s$, leading to

$$g_{\nu\nu}\frac{\mathrm{d}s^\nu}{\mathrm{d}s} + s^\nu\frac{\mathrm{d}g_{\nu\nu}}{\mathrm{d}s} = \frac{1}{2}\Big[(s^\nu)^2\, \partial_\nu g_{\nu\nu} + (s^\tau)^2\, \partial_\nu g_{\tau\tau}\Big]. \tag{29}$$

Division of this equation by $g_{\nu\nu}$ and using (Equation 25) provide the differential equation for $\mathrm{d}s^\nu/\mathrm{d}s$:

$$\begin{aligned} \mathrm{d}s^\nu/\mathrm{d}s &= -s^\nu\, g^{\nu\nu}\, \frac{\mathrm{d}g_{\nu\nu}}{\mathrm{d}s} + \frac{1}{2}(s^\nu)^2 g^{\nu\nu}\, \partial_\nu g_{\nu\nu} + \frac{1}{2}(s^\tau)^2\, g^{\nu\nu}\, \partial_\nu g_{\tau\tau} \\ &= -\frac{1}{2}(s^\nu)^2\, \sqrt{g^{\nu\nu}}\, \mathcal{D}_\nu g_{\nu\nu} + \frac{1}{2}(s_\tau)^2 (g^{\tau\tau})^2\, \sqrt{g^{\nu\nu}}\, \mathcal{D}_\nu g_{\tau\tau}. \end{aligned} \tag{30}$$

We write this equation as

$$\mathrm{d}s^\nu/\mathrm{d}s = a + b\,(s^\nu)^2, \quad \text{with} \quad \begin{cases} a = g^{\tau\tau}(s_\tau)^2\, \sqrt{g^{\nu\nu}}\ \mathcal{D}_\nu \ln\left(\sqrt{g_{\tau\tau}}\right), \\ b = -\dfrac{1}{2}\sqrt{g^{\nu\nu}}\ \mathcal{D}_\nu g_{\nu\nu}. \end{cases} \tag{31}$$

5.1. Construction of the Geodesics

We start with the integration of relation of (Equation 31) and assume that the geodesic is subdivided into a number of *curved* line segments with start point $\boldsymbol{x}(p-1)$ and end point $\boldsymbol{x}(p)$, $p = 1, 2, \ldots$. The position of this end point is yet unknown, but we require that the arc length along the geodesic curve between these two points is equal to the prescribed optical length Δs. Note that a function depending on $\boldsymbol{x}(p)$ will be written as a function of p, for example, $g_{\nu\nu}(\boldsymbol{x}(p)) = g_{\nu\nu}(p)$. We introduce a local arc-length parameter s that runs from $s(p-1) = (p-1)\Delta s$. The local coordinate x^ν runs from to $x^\nu(p-1)$ to $x^\nu(p-1) + \Delta x^\nu(p)$. Using the definition $s^\nu = \mathrm{d}x^\nu/\mathrm{d}s$ and integrating along s we obtain

$$\Delta x^\nu = \int_0^{\Delta s} s^\nu \, \mathrm{d}s, \tag{32}$$

in which $s^\nu = s^\nu(s)$. To obtain the curve of the geodesic we first determine the arc length as function of s^ν. We invert both sides of the first relation of (Equation 31), transfer $\mathrm{d}s^\nu$ to the other side and integrate with respect to s^ν. This results into the arc-length parameter s as

$$s = \int_{s^\nu(p-1)}^{s^\nu} \frac{1}{a + b\,(s^\nu)^2} \, \mathrm{d}s^\nu, \quad \text{where } s^\nu(p-1) \le s^\nu \le s^\nu(p). \tag{33}$$

We now assume that a and b are constant along the curved segment. The integration can be carried out analytically and provides us the parameter s as function of s^ν, viz.,

$$s = \frac{1}{\sqrt{ab}}\left[\arctan\left(\sqrt{b/a}\; s^\nu\right) - \arctan\left(\sqrt{b/a}\; s^\nu\right)\right], \tag{34}$$

where s runs from 0 to Δs. Multiplying both sides of (Equation 34) by $\sqrt{ab}$ and reordering the terms lead to

$$\arctan\left(\sqrt{b/a}\; s^\nu\right) = \sqrt{ab}\,\Delta s + A(p), \quad \text{with } A(p) = \arctan\left(\sqrt{b/a}\; s^\nu(p)\right). \tag{35}$$

After inversion we arrive at $s^\nu = \sqrt{a/b}\tan\left(\sqrt{ab}\; s + A(p)\right)$. We now conclude that we have an expression that enables us to compute Δx^ν. We substitute this expression into (Equation 32) and we use again that a and b along the curved segment and after an analytical integration the result is obtained as

$$\begin{aligned} \Delta x^\nu(p) &= -\frac{1}{b}\ln\left[\frac{\cos(\sqrt{ab}\;\Delta s + A(p))}{\cos(A(p))}\right], \\ &= -\frac{1}{b}\ln\left[\cos\left(\sqrt{ab}\;\Delta s\right) - \sqrt{b/a}\; s^\nu(p)\sin\left(\sqrt{ab}\;\Delta s\right)\right]. \end{aligned} \tag{36}$$

Note that for sufficiently small Δs this expression simplifies to $\Delta x^\nu(p) = s^\nu(p)\,\Delta s$.

The tangential component of $\boldsymbol{s}$ is updated as $s^\tau(p) = s^\tau(p-1) + \Delta x^\tau(p)$. To determine $\Delta x^\tau(p)$ we use the definition $s^\tau = \mathrm{d}x^\tau/\mathrm{d}s$ and the first relation of (Equation 28), and obtain $\Delta x^\tau(p) = g^{\tau\tau}(p)\, s_\tau\, \Delta s$. At the other hand we have $\Delta x^\nu(p) = s^\nu(p)\,\Delta s$. Hence we immediately see that

$$\Delta x^\tau(p) = [g^{\tau\tau}(p)\, s_\tau / s^\nu(p)]\, \Delta x^\nu(p), \tag{37}$$

where we have assumed that $g^{\nu\nu}$ and $g^{\tau\tau}$ are constant on the curved line element.

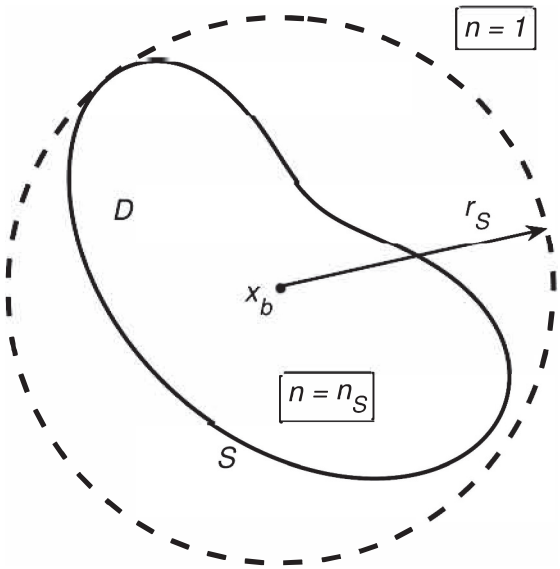

Figure 2. Inhomogeneous object with boundary S (solid curved line) enclosing a domain D, with refractive index n_S and a circumscribing sphere (dashed curve) with radius r_S.

6. The Refractional Tension

In this section we investigate how the tension **f** is related to the inhomogeneous distribution of the refractive index in the medium. In our previous paper, Fokkema and Van den Berg (2020), we have shown that there exists a refractional potential that satisfies (Equation 12). Using (Equation 11) this scalar potential function is related to the internal refractive index by the volume-integral representation

$$\Phi(\boldsymbol{x}) = 3\int_{\boldsymbol{x}'\in\mathcal{R}^3} \frac{n_S(\boldsymbol{x}')-1}{4\pi|\boldsymbol{x}-\boldsymbol{x}'|}\,\mathrm{d}V, \quad \boldsymbol{x}\in\mathcal{R}^3, \tag{38}$$

in which $(n_S(\boldsymbol{x}')-1)/(4\pi|\boldsymbol{x}-\boldsymbol{x}'|)$ can be considered as the field from a contrast source in the point $\boldsymbol{x}'$. The representation can be considered as a superposition of contrast sources for all points $\boldsymbol{x}'$. Next, we consider an object D with a refractive index $n_S(\boldsymbol{x})$ embedded in vacuum. The enclosing boundary is denoted as S, see Figure 2. The sources of contrast within the object generate, due to the difference of the refractive index with respect to unity, a force–refractional tension - inside and outside the object. Once a geodesic has been constructed, we discuss the group velocity and energy transfer along a curved segment of the geodesic between the points with arc-length parameters $s(p-1)$ and $s(p)$.

6.1. Expansion in Moments

In this paper, our main emphasis is on the construction of the geodetic path around the object where the detailed distribution of n_S is less important. Therefore, we define a barycenter $\boldsymbol{x}_b$ of the contrast-source distribution as origin of the coordinate system. The boundary enclosing D is denoted as S, see Figure 2. Then we write the distance as $\boldsymbol{x}-\boldsymbol{x}' = (\boldsymbol{x}-\boldsymbol{x}_b)-(\boldsymbol{x}'-\boldsymbol{x}_b)$ and we expand the free-space Green's function in powers of the inverse distance $|\boldsymbol{x}-\boldsymbol{x}_b|$ as

$$G(\boldsymbol{x}-\boldsymbol{x}_b) = \frac{1}{4\pi|\boldsymbol{x}-\boldsymbol{x}_b|}\left[1+\frac{(\boldsymbol{x}-\boldsymbol{x}_b)\cdot(\boldsymbol{x}'-\boldsymbol{x}_b)}{|\boldsymbol{x}-\boldsymbol{x}_b|^2}+O\left(\frac{|\boldsymbol{x}'-\boldsymbol{x}_b|^3}{|\boldsymbol{x}-\boldsymbol{x}_b|^2}\right)\right]. \tag{39}$$

For points outside the circumscribed sphere, we substitute this expansion into (Equation 38) and interchange integration and summation. This leads to the field expression

$$\Phi = \frac{M^{(0)}}{4\pi|\boldsymbol{x}-\boldsymbol{x}_b|}+\frac{(\boldsymbol{x}-\boldsymbol{x}_b)\cdot\mathbf{M}^{(1)}}{4\pi|\boldsymbol{x}-\boldsymbol{x}_b|^2}+O\left(\frac{|\boldsymbol{x}'-\boldsymbol{x}_b|^2}{|\boldsymbol{x}-\boldsymbol{x}_b|^3}\right), \quad |\boldsymbol{x}-\boldsymbol{x}_b|>R_S, \tag{40}$$

with monopole moment and dipole moment, defined as

$$M^{(0)} = 3\int_{\boldsymbol{x}\in D}[n_S(\boldsymbol{x}')-1]\,\mathrm{d}V \quad \text{and} \quad \mathbf{M}^{(1)} = 3\int_{\boldsymbol{x}\in D}[n_S(\boldsymbol{x}')-1](\boldsymbol{x}'-\boldsymbol{x}_b)\,\mathrm{d}V. \tag{41}$$

Hence, the expression for the potential Φ in the far-field region becomes the sum of a monopole term and a dipole term. In a similar way as in gravity, we define the barycenter as the point where the weighted integral of angular forces vanishes. In this paper, we introduce a refractional barycenter that follows from the condition

$$\int_{\boldsymbol{x}'\in D}[n_S(\boldsymbol{x}')-1](\boldsymbol{x}'-\boldsymbol{x}_b)\,\mathrm{d}V = 0 \tag{42}$$

$$\boldsymbol{x}_b = \int_{\boldsymbol{x}'\in D}[n_S(\boldsymbol{x}')-1]\boldsymbol{x}'\,\mathrm{d}V \Big/ \int_{\boldsymbol{x}'\in D}[n_S(\boldsymbol{x}')-1]\,\mathrm{d}V. \tag{43}$$

Note that the expression for $M^{(1)}$ vanishes as the condition of (Equation 42) is satisfied by choosing the barycenter expression of (Equation 43). Then the dipole term vanishes and only the higher order multi-pole contributions in the expansion are neglected. We may assign the potential Φ and the tension $\mathbf{f} = -\nabla\Phi$ as

$$\Phi = \frac{M^{(0)}}{4\pi|\boldsymbol{x}-\boldsymbol{x}_b|} + O\left(\frac{|\boldsymbol{x}'-\boldsymbol{x}_b|^2}{|\boldsymbol{x}-\boldsymbol{x}_b|^3}\right), \qquad \boldsymbol{f} = \frac{M^{(0)}}{4\pi|\boldsymbol{x}-\boldsymbol{x}_b|^2}\frac{\boldsymbol{x}-\boldsymbol{x}_b}{|\boldsymbol{x}-\boldsymbol{x}_b|} + O\left(\frac{|\boldsymbol{x}'-\boldsymbol{x}_b|^3}{|\boldsymbol{x}-\boldsymbol{x}_b|^4}\right). \tag{44}$$

Note that within the present approximation, the potential Φ depends only on the radial coordinate $r = |\boldsymbol{x} - \boldsymbol{x}_b|$ with the barycenter as origin.

For a radially layered medium, the tension of (Equation 44) is valid in the exterior and interior domain of the object. It is directed in the radial direction. Its amplitude f is obtained as

$$f = \frac{3}{r^2}\int_0^r [n_S(r')-1]\,(r')^2\,\mathrm{d}r', \quad r \in \mathcal{R}^3. \tag{45}$$

6.2. Group Velocity and Intensity Evolution on the Geodesic

Before we discuss the electromagnetic wavefield that propagates along the geodesic, we note that the electromagnetic wavefield in our present configuration is given by the integral equation, see Abubakar and Van den Berg (2004) and Van den Berg (2021),

$$\boldsymbol{E}(\boldsymbol{x}) = \boldsymbol{E}_0(\boldsymbol{x}) + \left(k^2 + \nabla\nabla\cdot\right)\int_{\boldsymbol{x}'\in D} \frac{\exp(\boldsymbol{i}\,k\,|\boldsymbol{x}-\boldsymbol{x}'|)}{4\pi|\boldsymbol{x}-\boldsymbol{x}'|}(n_S-1)\,\boldsymbol{E}(\boldsymbol{x}')\,\mathrm{dV}, \tag{46}$$

in which $\boldsymbol{i}$ is the imaginary unit, $k = \omega/c_0$ is the wave number, ω is the radial frequency of the wavefield, $\boldsymbol{E}$ is the electric-field vector, and $\boldsymbol{E}_0$ is the electric-field vector in the vacuum embedding in absence of the contrasting object ($n_S = 1$). Note that this equation is valid for unit electromagnetic permeability. We observe that the kernel of this integral equation has a convolution structure in space. The exponential function represents the propagation between the observation point point $\boldsymbol{x}$ and the contrast source at $\boldsymbol{x}'$. The total field is a weighted summation over all contrast sources. This weighting factor $1/(4\pi|\boldsymbol{x}-\boldsymbol{x}'|)$ does not depend on the wave number and leads to a spatial deformation of the wavefield. This is exactly the dispersion factor of the potential-field representation of (Equation 38). The operator $(\nabla\,\nabla\,\cdot)$ represents the anisotropic nature of the electromagnetic field in the vicinity of the object D. This is commonly noted as polarization.

When we are interested in the propagation path of least action, independent of the frequency, the determination of the geodesic from the potential-field representation is justified. Once the geodesic is determined, the propagation factor $\exp(\boldsymbol{i}\,k\,\Delta s)$ outside the object D and the group velocity is discussed. In general the group velocity along the geodesic in a space with spatial dispersion is defined as

$$v_{\mathrm{g}} = \frac{\mathrm{d}\omega}{\mathrm{dk}} = \frac{\mathrm{d}l}{\mathrm{d}s}c_0, \quad \text{with} \quad \mathrm{d}l = \sqrt{(\mathrm{d}x^\nu)^2 + (\mathrm{d}x^\tau)^2}, \tag{47}$$

where $\mathrm{d}l$ is the differential path length in Riemannian space and $\mathrm{d}s$ is the optical length, see (Equation 1). From (Equation 47) it follows that $\mathrm{d}s/c_0 = \mathrm{d}l(s)/v_{\mathrm{g}}(s)$ compared to $\mathrm{d}s/c_0 = \mathrm{d}l(\boldsymbol{x})/c(\boldsymbol{x})$, see (Equation 2). The propagation factor along the geodesic is $\exp(\boldsymbol{i}\,k\,\Delta s) = \exp(\boldsymbol{i}\,2\pi\Delta s/\lambda)$. The group velocity v_{g} follows from (Equation 47) and using (Equation 28) as

$$v_{\mathrm{g}}/c_0 = \sqrt{g^{\nu\nu} + (s_\tau)^2\,g^{\tau\tau}(g^{\tau\tau} - g^{\nu\nu})}. \tag{48}$$

The time average of the total energy density $\langle w\rangle$ is propagating with the group velocity v_{g} along the geodesic. From (Equation 18) it readily follows that

$$g_{\nu\nu}\left(v_{\mathrm{g}}^{\nu}\right)^2 + g_{\tau\tau}\left(v_{\mathrm{g}}^{\tau}\right)^2 = c_0^2, \tag{49}$$

which shows how the local group velocity v_g is related to the constant phase velocity c_0, which is the essence of Einstein's theory. The propagation of the energy density vector is known as the Poynting vector $\mathbf{S}(\boldsymbol{x})$ where $\boldsymbol{x}$ is a function of the direction vector $\boldsymbol{s}$, is given by see Born and Wolf (1959), Equation 23 on page 113, viz.,

$$\langle \mathbf{S} \rangle = I(s)\,\boldsymbol{s} = v_g \langle w \rangle \boldsymbol{s}. \tag{50}$$

The intensity $I(s) = v_g \langle w \rangle$ along the geodesic is defined as the absolute value of the time average of the Poynting vector. The conservation of energy along the geodesic requires $I(s)\boldsymbol{s} = \text{constant} = I(0)\boldsymbol{s}(0)$, where $I(0)$ is the intensity at the starting point of the geodesic. This allows for the introduction of the normalized energy density $\mathcal{E}$ along the geodesic, see (Equation 48),

$$\mathcal{E} = \langle w \rangle / \langle w \rangle(0) = c_0 / v_g, \tag{51}$$

where $\langle w \rangle\,(0)$ is the average value of the total energy density w at the starting point of the geodesic. In geometric optics $g_{\nu\nu} = g_{\tau\tau} = n^2$ and we have $\mathcal{E} = n$. Note that $\mathcal{E}$ is the inverse of the group velocity v_g. This expresses the intuitive fact that for fixed intensity, a reduced group velocity corresponds to a higher stored energy density. Along the geodesic, refractive-index gradients (manifestations of local metric curvature) drive a continual exchange between kinetic and potential energy, and it is this curvature-induced imbalance that dictates the trajectory.

It is interesting to investigate $\mathcal{E}$ in the perihelion at $\boldsymbol{x}_{\text{per}}$. In the perihelion of the geodesic, where the distance to the barycenter is minimal, we have $s^\nu = 0$ and $g^{\tau\tau}(s_\tau)^2 = 1$. Then we have $\mathcal{E}(\boldsymbol{x}_{\text{per}}) = \sqrt{g_{\tau\tau}(\boldsymbol{x}_{\text{per}})}$. Further in the perihelion where $s^\nu = 0$, from (31) we conclude that $\mathrm{d}s^\nu/\mathrm{d}s = a$ and the curvature K in the perihelion $\boldsymbol{x}_{\text{per}}$ becomes, $K(\boldsymbol{x}_{\text{per}}) = \sqrt{g_{\nu\nu}}\,\mathrm{d}s^\nu/\mathrm{d}s = \sqrt{g_{\nu\nu}}\,a = \mathcal{D}_\nu \ln\sqrt{g_{\tau\tau}(\boldsymbol{x}_{\text{per}})}$, cf. Born and Wolf (1959), Equation 14 on p. 123. Note that in the perihelion, the curvature can be written as $K = \mathcal{D}_\nu \mathcal{E}/\mathcal{E}$, which shows the relation between the curvature and intensity in the perihelion where the geodesic experiences the largest curvature.

6.3. Homogeneous Sphere

In Section 6.1, we observed that for an arbitrary spatial distribution of the refractive index, the resulting refractional tension arises as the superposition of individual monopole contributions. In astrophysical contexts, the objects of interest are typically spherical and exhibit a radially symmetric inhomogeneous refractive index. Based on the preceding discussion, we may conclude that the corresponding refraction potential and tension can be effectively described by a simple monopole. Notably, the form of the refraction potential closely resembles that of Newton's gravitational potential. Since $s^\nu = \mathrm{d}r/\mathrm{d}s$, $s^\tau = r\,\mathrm{d}\theta/\mathrm{d}s = r\,s^\theta$, by defining $s^\theta = \mathrm{d}\theta/\mathrm{d}s$, the relation between the components of the metric tensor of (Equation 27) is now obtained as

$$g_{\nu\nu}\,(s^\nu)^2 + g_{\tau\tau}\left(s^\theta\right)^2 = 1, \quad \text{with} \quad g_{\nu\nu} = \left(1/\lambda^{(\nu)}\right)^2,\ g_{\tau\tau} = \left(r/\lambda^{(\tau)}\right)^2. \tag{52}$$

Note that now the dimension of $g_{\tau\tau}$ is $\left[\mathrm{m}^2\right]$. The relations of (Equation 28) are written as

$$s^\theta = g^{\tau\tau} s_\theta\,, \quad s^\nu = \sqrt{g^{\nu\nu}}\sqrt{1 - g^{\nu\nu}(s_\theta)^2}, \tag{53}$$

where s_θ is constant. To simplify our further analysis, we consider a spherical object with constant refractive index n_S. We use a spherical coordinate system, where $r = |\boldsymbol{x}|$ and the barycenter is located at the origin $\boldsymbol{x} = \mathbf{0}$ of this coordinate system. The outer radius of this object is denoted as r_S. The refractional tension f follows from (Equation 45) and

$$f/r = \begin{cases} (n_S - 1), & r \le r_S, \\ (n_S - 1)\, r_S^3/r^3, & r \ge r^S. \end{cases} \tag{54}$$

Using (Equation 16) and (Equation 17) the components of the metric tensor are obtained as

$$\begin{cases} g_{\nu\nu} = 1/n_S^2, & g_{\tau\tau} = r^2/n_S^2, & r < r^S, \\ g_{\nu\nu} = [1 - 2f/r]^{-2}, & g_{\tau\tau} = r^2[1 + f/r]^{-2}, & r > r_S. \end{cases} \tag{55}$$

Note that the tension f and the metrical component $g_{\tau\tau}$ are continuous at $r = r_S$, while the component $g_{\nu\nu}$ jumps in the radial direction at the boundary of the sphere. We write the first relation of (Equation 53) as $s_\theta = g_{\tau\tau}\, r^2\, s^\theta$ and observe that this relation holds everywhere, in particular in the starting point. The increment of Δr follows from (Equation 36) and the increment of $\Delta\theta$ follows from (Equation 37). The computation of coefficients a and b for the sphere are straightforward and leads to

$$a = 3\,(s_\theta/r)^2\sqrt{g^{\nu\nu}\, g^{\tau\tau}}\,(n_S - 1)\, r_S^3/r^4, \quad \text{and} \quad b = 6\, g_{\nu\nu}\,(n_S - 1)\, r_S^3/r^4. \tag{56}$$

6.4. Construction of Harmonic Wave Propagation Along a Geodesic

To obtain the position points in Cartesian space, we use

$$x_1(p) = r(p)\cos(\theta(p)) \quad \text{and} \quad x_2(p) = r(p)\sin(\theta(p)). \tag{57}$$

Now we can plot the geodetic curve through the points $\boldsymbol{x}(p)$. Further, we want to illustrate the propagation of a harmonic wave along this geodesic. Therefore, we determine the direction vector $\boldsymbol{s}$ along this curve in Cartesian space. We have

$$\Delta x_1(p) = x_1(p+1) - x_1(p) \quad \text{and} \quad \Delta x_2(p) = x_2(p+1) - x_2(p), \tag{58}$$

with distance $\text{norm}[\Delta x(p)] = \sqrt{(\Delta_1(p))^2 + (\Delta_2(p))^2}$ and construct the unit vector $\boldsymbol{s}$ in the direction of propagation as

$$s_1(p) = \Delta x_1(p)/\text{norm}[\Delta x(p)] \quad \text{and} \quad s_2(p) = \Delta x_2(p)/\text{norm}[\Delta x(p)]. \tag{59}$$

The unit vector normal $\boldsymbol{n}$ to the direction of propagation is obtained from $n_1 s_1 + n_2 s_2 = 0$ as $n_1(p) = -s_2(p)$ and $n_2(p) = s_1(p)$. We now define the harmonic wave along the geodesic as a function of the arc length $s = s(p)$, which is given by (Equation 34). The amplitude is given as

$$A(p) = A\cos\left[\frac{2\pi}{\lambda}s(p)\right]. \tag{60}$$

We plot the harmonic wave as a distortion of the geodesic in the direction normal to the geodetic path. The amplitude A is the wave amplitude at the start point of the geodesic, while λ is the wavelength at this point. In our numerical results we take $A = 0.30$ and $\lambda/r_S = 0.25$. The coordinates of the wave follow from geodesic coordinates as

$$x_1^{\text{w}}(p) = x_1(p) + A(p)\, n_1(p) \quad \text{and} \quad x_2^{\text{w}}(p) = x_2(p) + A(p)\, n_2(p). \tag{61}$$

The curve plotted through these points $\boldsymbol{x}^{\text{w}}(p)$ illustrates the propagation features along the geodesic. If we choose a constant amplitude $A(p) = A$ along the geodesic, we do not take into account the energy change along the propagation path and we only observe a change of the local wavelength at $\boldsymbol{x}^{\text{w}}(p)$ as function of p, because $s(p)$ changes. During the propagation the amplitude must change as well, because the energy $\mathcal{E}$ contained in the wave is equal to $v_g(0)/v_{\text{g}}(p)$. Therefore we select. $A(p) = A\,\mathcal{E} = A\, v_{\text{g}}(0)/v_{\text{g}}$.

6.5. Numerical Results

We only consider geodesics starting in the horizontal x_1-direction. At the start point we have $r(0) = \sqrt{x_1^2(0) + x_2^2(0)}$ and $\theta(0) = \pi - \arcsin(x_2(0)/r(0))$, so that

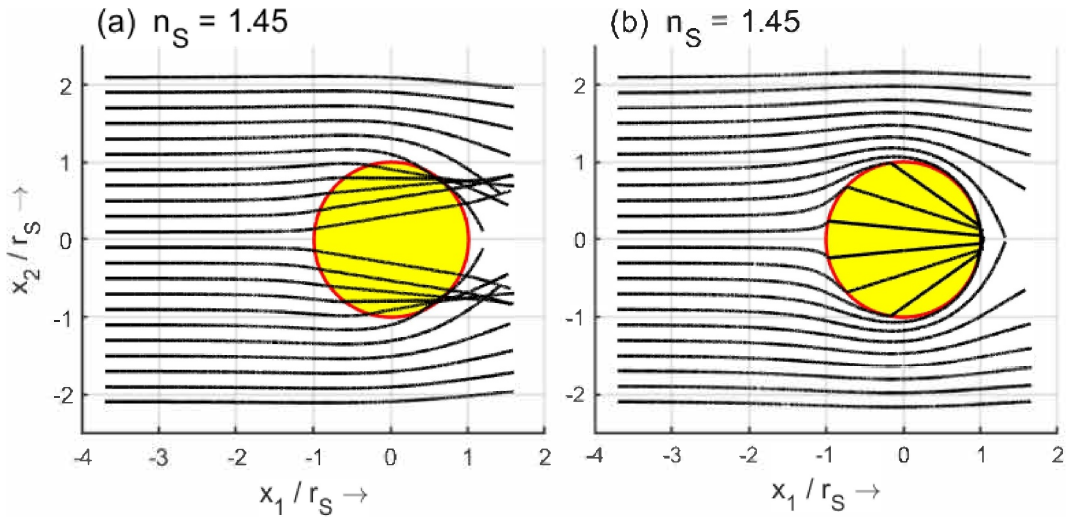

Figure 3. Comparison of geodesics in presence of a homogeneous sphere; (a) scalar analysis of Fokkema and Van den Berg (2019) and (b) tensor analysis of present paper.

$$f(0)/r(0) = (n_S - 1)/r^3(0) \quad \text{and} \quad s_\theta(0) = x_2(0)/(1 + f(0)/r(0)). \tag{62}$$

In Figure 3, we start with a homogeneous sphere and internal refractive index $n^S = 1.45$. We compare the geodesics based on the scalar theory of the geodesics (Figure 3a) and the one using the tensor theory of the present paper (Figure 3b). Each geodesic starts at the horizontal coordinate $x_1(0)/r_S = -3.7$ and has a normalized arc length s/r_S of 5.3. The coordinates x_2 of the starting points of the geodesics are located symmetrically in the vertical direction. The construction of the geodesics in Figure 3a are explained in Fokkema and Van den Berg (2019). In the domain outside the sphere, we observe that the geodesics initially bend away from the horizontal axis $x_2 = 0$. While passing the sphere they bend toward the sphere, except for the geodesics crossing its interior domain. In Figure 3b, the start position and the direction are known and the next point is computed by using (Equation 36) and (Equation 37), together with (Equation 56). This procedure is repeated and the geodesic is visualized by plotting the line segments connecting all the points $\boldsymbol{x}$. The geodesics in Figure 3b exhibit a more flexible reaction on the presence of the sphere. For this value of n_S, the homogeneous sphere has a remarkable focusing effect. In the remainder of this section we concentrate on the particular features that follow from our present analysis.

In Figure 4, for various values of the interior refractive index, we show the geodesics and their wavefronts. These wavefronts are visualized by plotting the line segments connecting all the points of each geodesics with the same arc length $s(p)$. These values of $s(p)$ are obtained by updating the arclength by using $s(p) = s(p-1) + \Delta s$. In Figure 4a, for $n_S = 1.2$, the spatial dispersion of our Riemannian space is clearly visible in the spatial deformation of the wave front in the positive horizontal direction, and the bending of the geodesics close to the sphere. This effect is magnified by increasing n_S. In Figure 4b, we consider $n_S = 1.45$. In front of the left-side of the sphere we observe a stagnation in the propagation of the wavefront, indicating the presence of a group of waves with a velocity less than c_0. Instead of *time dispersion*, we are dealing with *spatial dispersion* by the presence of the refractive object. Even at a vertical level of $|x_2|/r_S = 2$ the deformation of space due to the tension f is still visible.

What happens in the perihelion? In the perihelion, the normalized energy and the curvature are given by

$$\mathcal{E}(r_{\text{per}}) = \frac{1}{1 + (n_S - 1)\, r_S^3/r_{\text{per}}^3} \quad \text{and} \quad K(r_{\text{per}}) = \frac{3(n_S - 1)\, r_S^3/r_{\text{per}}^4}{1 + (n_S - 1)\, r_S^3/r_{\text{per}}^3}. \tag{63}$$

and for the case that $r_{\text{per}} = r_S$ we have $\mathcal{E}(r_S) = 1/n_S$ and $K(r_S) = 3(n_S - 1)/(n_S\, r_S)$. Note that for $n_S \le 1.5$ the curvature is $K(r) \le 1/r_S$. A further increase of the refractive index to values of $n_S > 1.5$ leads not only to higher

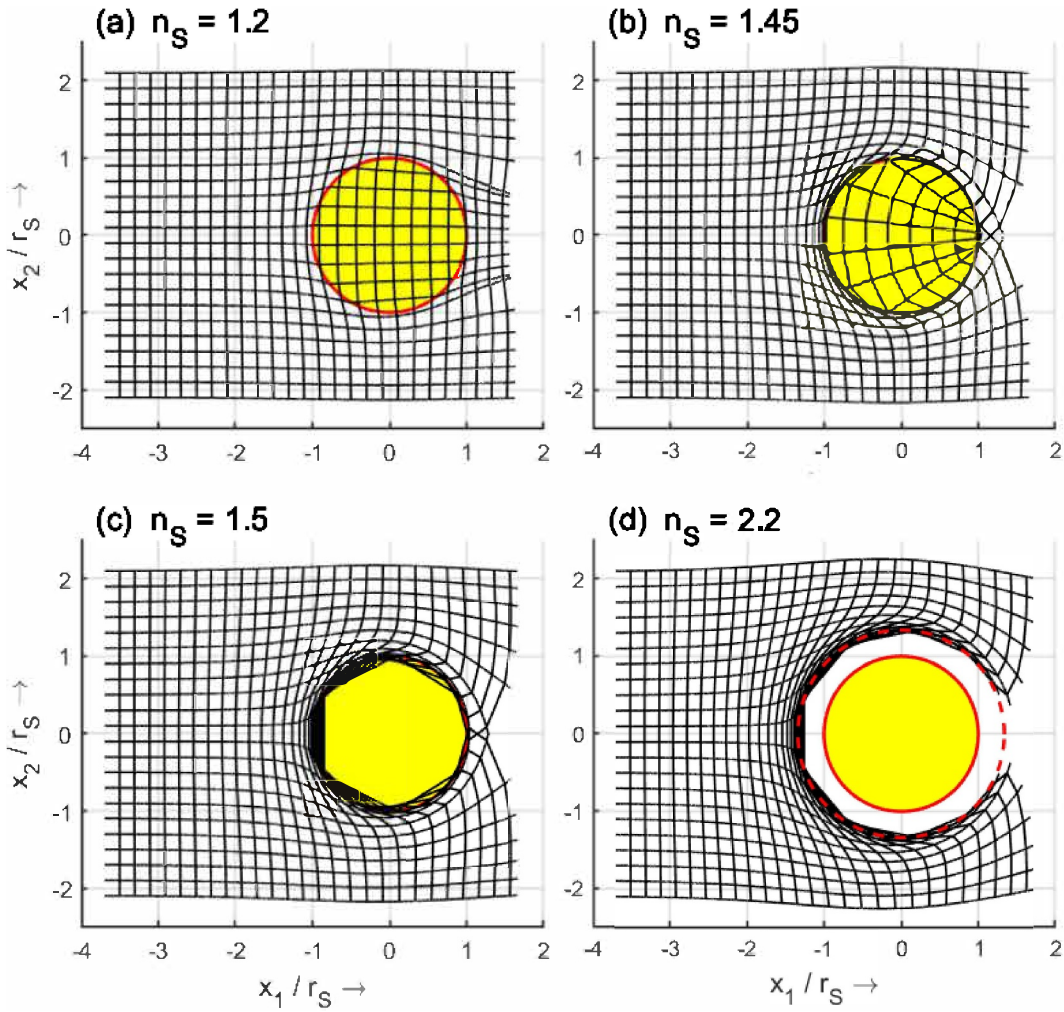

Figure 4. Geodesics and wave fronts in presence of the sphere with $n_S = 1.2$, 1.45, 1.5, and 2.2, respectively. The red dashed circle denotes the radius r_{crit} where $g^{rr} = 0$.

values of the curvature, but also to another point of attention. The eigenvalue $\lambda^{(\nu)}$ may vanish outside the sphere and $g^{rr} = 0$ for $r/r_S \geq 1$. Therefore, we define a critical radius r_{crit} as the radius where the radial component of the metric tensor g^{rr} vanishes. From the second relation of (Equation 53) it follows that $r_{\text{crit}}/r_S = [2(n_S - 1)]^{\frac{1}{3}}$.

What happens in the critical radius? In Figure 4c, we increase n_S slightly, viz., $n_S = 1.5$, so that the critical radius is equal to the radius of the sphere. No wave can propagate through this sphere and it will continue in the angular direction and it rotates along the spherical circle with radius r_{crit}. Increasing the internal refractive index n_S to higher values means that the wave cannot even enter the spherical domain between $r_S < r < r_{\text{crit}}$. This is visualized in Figure 4d, where $n_S = 2.2$. In the latter case, we have $r_{\text{crit}}/r_S = 1.34$. We remark that physically no wave propagation is possible in the radial direction. Mathematically, it means that matrix C_{ij} has a zero eigenvalue with respect to the radial coordinate and multiplication of C_{ij} by this eigenvector results into in a non-zero vector. The 3D space of transformation reduces to a 2D space spanned by the angular coordinates and at the critical radius the propagation continues in the angular direction.

What happens with the energy $\mathcal{E}$ and curvature K? At the critical radius, we have $\mathcal{E}(r_{\text{crit}}) = 2/3$ and $K(r_{\text{crit}}) = 1/r_{\text{crit}}$ The touching point fits perfectly to the critical radius and 1/3 of the normalized intensity is necessary for the bending around the sphere.

In Figure 5 we return to our geodesics outside the sphere for $n_S = 1.45$ and 2.2. The start points in the x_1-direction are at $x_1/r_S = -7$. In this figure we show how a harmonic wave propagates along geodesics. At this point, we

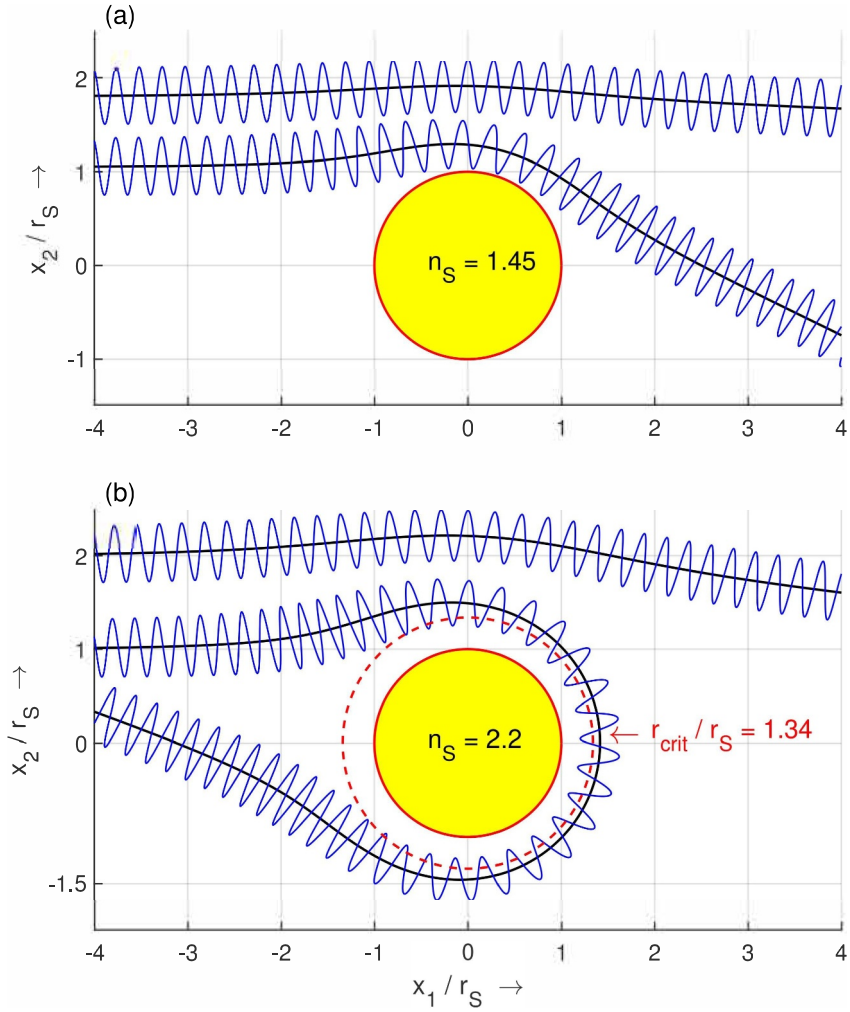

Figure 5. Geodesics and harmonic-wave propagation along the geodesic outside the sphere for $n_S = 1.45$ and 2.2.

note that the geodesic is symmetric with respect to the location of the perihelion. This means that after determination of the perihelion, we only have to construct the geodesic between start point and perihelion. The other part can be obtained by mirroring. In Figure 5a, the critical radius is less than r_S. In the neighborhood of the perihelion, where the geodesic has the smallest distance to the barycenter of the sphere, an increase of the local wavelength together with a decrease of the amplitude occur. In fact, the wave looses it energy, which is recovered when the wave propagates away from the sphere.

In Figure 5b, where the critical radius is greater than r_S, we observe that the geodesic, close to the sphere, rotates almost along the critical radius, but has enough energy to propagate away from the sphere, while recovering the energy. Further note that the perihelion is located at the right-hand side of the sphere at $x_1 = 1.39$ and $x_2 = -0.24$. The line through this perihelion point and the origin of the coordinate system is the line of symmetry of the geodetic in the (x_1, x_2)-plane. At the left-hand side, there is another intersection point of the geodesic and the line of symmetry, viz., at $x_1 = -5.69$ and $x_2 = 1.00$. Further we observe that the bending of a monochromatic wave along a geodesic may be visualized by analogy with a mechanical spring drawn around a fixed rod. The elongation and compression of the coils represent the local redistribution of energy density as the wave/coil adapts to the curvature of the trajectory.

In Figure 6, the propagation along the geodesic in the horizontal direction starting at $x_1(0)/r_S = -7$ is given for $n_S = 1.45$ and 2.2. Note that in Figure 6a toward the sphere, both the amplitude of the wave and local oscillations increase. Inside the sphere the amplitude and oscillation are constant. Note that the behavior is symmetric with

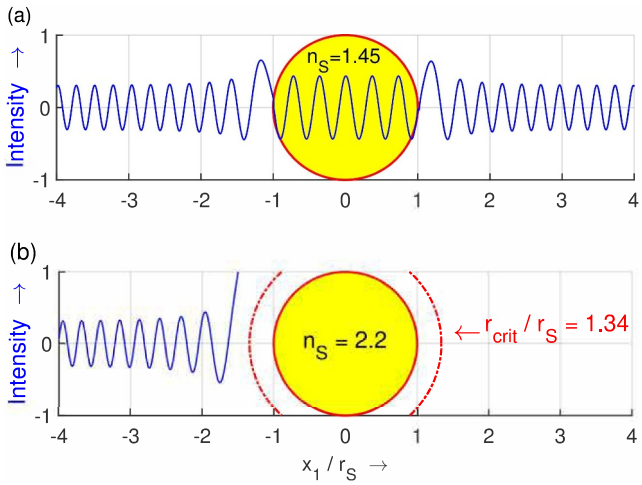

Figure 6. Geodesic along horizontal x_1-axis for $n_S = 1.45$ and 2.2.

respect to the origin. In Figure 6b, the wave propagation in the positive direction stops at the critical radius. At this position the wave will return as a reflected wave.

7. Applications

In this section, we present an astrophysical and an optical application, where the knowledge of the geodetic path is essential.

7.1. Shapiro's Two-Way Time

Irwin Shapiro's groundbreaking work, see Shapiro (1964), Shapiro et al. (1968), Shapiro (1971), Shapiro et al. (1977), demonstrated that radio astronomy could provide a fourth classical test of Einstein's theory of general relativity. This test relies on measuring the two-way travel time of a radar pulse transmitted from Earth, reflected by a planetary body, and received back at the transmitter. When the radar beam passes through the gravitational field of a massive object, its travel time increases. This Shapiro time delay directly reflects the strength of the intervening gravitational potential. Within general relativity, such delays arise because light follows curved geodesics in a non-Euclidean space–time geometry, rather than being acted upon by classical forces. This geometric interpretation also underlies the famous prediction of starlight deflection near the Sun, confirmed repeatedly by astronomical measurements. In our work we present a complementary perspective. We show that the deflection and delay of electromagnetic signals can also be described as spatial dispersion, arising when the propagating wavefront experiences refractional tension in the vicinity of a massive object. Consider the configuration illustrated in Figure 7. An electromagnetic signal is sent from the emitter position $\boldsymbol{x}_E$ to a moving monitor at $\boldsymbol{x}_M$, where it is reflected and sent back to $\boldsymbol{x}_E$. The total elapsed time upon return defines the Shapiro two-way time. To quantify this effect, we first introduce the differential path length $\mathrm{d}l = \sqrt{(\mathrm{d}x^\nu)^2 + (\mathrm{d}x^r)^2}$, and from this we define the differential two-way Shapiro time $\mathrm{d}T$ as

$$\mathrm{d}T = 2\left(\frac{\mathrm{d}l}{v_g} - \frac{\mathrm{d}l}{c_0}\right) = 2\left(\frac{c_0}{v_g} - 1\right)\frac{\mathrm{d}l}{c_0}, \tag{64}$$

where the normalized group velocity expression of (Equation 48) should be used. By construction, $\mathrm{d}T = 0$ when no object is present, (Equation 64) depends on absolute distances, which is impractical and prone to numerical uncertainty. Instead, it is more robust to examine the variation of $\mathrm{d}T$. For this purpose we consider the derivative of the elapsed time

$$\frac{\mathrm{d}T}{\mathrm{d}t}(r) = 2\left(\frac{c_0}{v_g} - 1\right)\frac{v_M(r)}{c_0}, \tag{65}$$

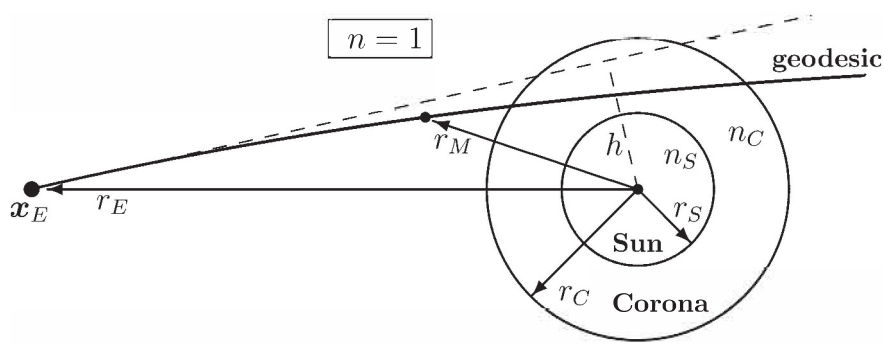

Figure 7. Configuration of the Shapiro measurement of the Sun, where r_S is the photometric radius of the Sun, r_C is the outer boundary of the Corona, and h is the perihelion distance to the barycenter, in absence of the Sun and Corona.

where the velocity of the monitor is introduced as $v_M = \mathrm{d}l/\mathrm{d}t$, following Misner et al. (2017), page 1106.

To account for a realistic solar environment, we consider a spherical layered object consisting of a dense body and an overlying Corona. The Corona is modeled between the photometric radius r_S of the Sun and its outer boundary r_C. The refractive indices are n_S and n_C, respectively. Using (Equation 45), we obtain the following expression for f/r,

$$f(r)/r = \begin{cases} (n_S - n_C)\, r_S^3/r^3, & r_S < r \le r_C, \\ (n_C - 1)\, r_C^3/r^3 + (n_S - n_C)\, r_S^3/r^3, & r \ge r_C. \end{cases} \tag{66}$$

Using (Equation 16) and (Equation 17) the components of the metric tensor are obtained as

$$\begin{cases} g_{vv} = [n_C - 2f/r]^{-2}, & g_{\tau\tau} = r^2[n_C + f/r]^{-2}, & r_S < r < r_C, \\ g_{vv} = [1 - 2f/r]^{-2}, & g_{\tau\tau} = r^2[1 + f/r]^{-2}, & r > r_C. \end{cases} \tag{67}$$

When the monitor is oriented toward the barycenter, the derivative of the returned signal, together with the known monitor velocity, allows direct determination of the geometric tensor, viz.,

$$\frac{\mathrm{d}T}{\mathrm{d}t}(r) = 2\left(\sqrt{g_{vv}(r)} - 1\right)\frac{v_M(r)}{c_0}. \tag{68}$$

At perihelion, the return signal becomes

$$\frac{\mathrm{d}T}{\mathrm{d}t}(r_{\mathrm{per}}) = 2\left(\sqrt{g_{\tau\tau}(r_{\mathrm{per}})} - 1\right)\frac{v_M(r_{\mathrm{per}})}{c_0}. \tag{69}$$

This result is directly relevant to contemporary missions. For instance, the Parker Solar Probe mission (http://parkersolarprobe.jhuapl.edu) launched in 2018 and operating until 2026, makes repeated perihelion passes at distances of less than $10\, r_S$ and a speed of the monitor of 0.064 % of the velocity of light. In such regimes, the transmitted signal traverses both the solar Corona and the deep gravitational potential of the Sun. Incorporating our refractive-dispersion model into the analysis of probe telemetry, see Sokol (2018), may therefore yield improved constraints on coronal density, refractive index, and the Sun's effective gravitational properties, see Sebástian et al. (2022).

7.2. Lüneburg Lens

We now consider the Lüneburg lens, see Lüneburg (1944) and Gómez et al. (2021), as example of a radially layered sphere. To simplify the formulas, we assume that that the radius $r_S = 1$. Its refraction index is then given by $n_S(r) = \sqrt{2 - r^2}$. The integral of (Equation 45) is computed analytically, so that.

$$f/r = \begin{cases} \dfrac{6\arcsin\left(r/\sqrt{2}\right) - 3\, n_S\left(n_S^2 - 1\right) r}{4r^3} - 1, & r \le 1, \\ \dfrac{(3\pi/8 - 1)}{r^3}, & r \ge 1, \end{cases} \tag{70}$$

and after calculation of the eigenvalues, see (Equation 52) and using (Equation 16) and (Equation 17), the metric tensor becomes

$$\begin{cases} g_{vv} = [1 + 3\,(n_S - 1) - 2f/r]^{-2}, & g_{\tau\tau} = r^2[1 + f/r]^{-2}, \quad r < 1, \\ g_{vv} = [1 - 2f/r\,]^{-2}, & g_{\tau\tau} = r^2[1 + f/r]^{-2}, \quad r > 1. \end{cases} \tag{71}$$

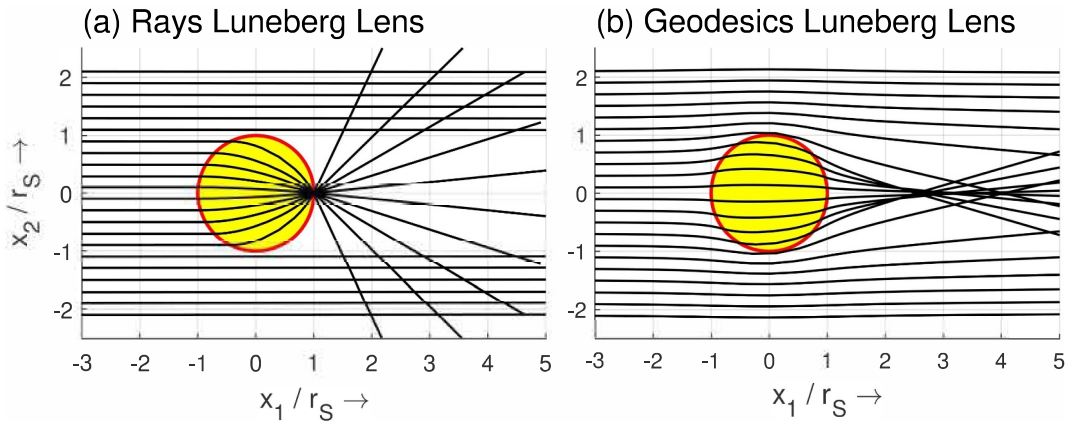

Figure 8. Wave trajectories through Lüneberg lens with $n_S = \sqrt{2 - r^2/r_S^2}$, based on (a) ray theory and (b) geodesic theory.

For comparison, we show in Figure 8a the rays in geometrical optics using ds of (Equation 3), by changing $g_{vv} = n_S^2$ and $g_{\tau\tau} = (r\,n_S)^2$ for $r < 1$, while enforcing f to zero for $r > 1$. In Figure 8b, we show the geodesics and illustrate the emergent nature of the refractive object. The incident plane wave bends around the sphere, while the geodesics entering the sphere intersect its surface with positions and angles that differ from those predicted by conventional ray optics. As a result, the focusing effect ordinarily associated with a lens is distorted, demonstrating that the emergent properties of refractive objects must be explicitly accounted for in lens design. These results further show that, owing to the invariance of the optical path length across different spatial frames, the local focusing effect of light propagation extends continuously from the interior to the exterior of the object. At the same time, the global propagation remains invariant, consistent with Einstein's principle.

To aid the reader, Figure 9 presents the Matlab code used to produce Figure 8b, demonstrating the effective simplicity of numerically implementing geodesics based on the principle of least action.

In the next section, we present an overview of the novelties and advantages of our proposed method.

8. Novelties and Advantages of the Proposed Method

1. *Simplified light-deflection analysis*.

Light deflection by a massive object, usually described via the space-time metric, can equivalently be formulated using macroscopic electromagnetic field equations in a spatial metric. This approach reduces tensor complexity and substantially lowers computational cost.

2. *Emergent spatial-dispersion interpretation*.

The deflection and delay of electromagnetic signals arise naturally as spatial dispersion: the propagating wavefront experiences refractional tension near the spatial inhomogeneity, effectively "sensing" the object before contact.

3. *Direct computation of local wave properties*.

With geodesics determined, the local arc length allows immediate calculation of wave velocity and amplitude along the path. Points at equal optical distance define the wavefront curvature, revealing the spatial distortion around the object.

4. *Global geodesic determination and inversion potential*.

The method specifies the entire geodesic structure from the spatial distribution of refractive indices. Two-way travel-time analysis along the geodesic yields the local potential-energy ratio, enabling inversion applications.

```
figure;  axis equal;  axis tight;  axis xy;  axis([-3 5 -2.5 2.5]);
title('Luneberg lens', 'Fontsize', 16);      hold on;    grid on;
xlabel('x_1 / r_S \rightarrow','Fontsize', 12)
ylabel('x_2 / r_S \rightarrow','Fontsize', 12)
xticks([-3 -2 -1 0 1 2 3 4 5]);  yticks([ -3-2 -1 0 1 2]);
phi = 0:0.01:2*pi; x = cos(phi); y = sin(phi);
plot(x,y,'-r','LineWidth',1.5);  fill(x,y,'y');  % plot sphere
% INPUT PARAMETERS
   p_end = 50000;                % number of points on the geodesic
      ds = 0.001;                % arc length ds
      X1 = -3.7;  X2 = 2.1;      % start position (x_1,x_2)
      nH = 22;    dH = 0.2;      % number and change of start value
% Initial radial coordinate r and angular coordinate t = theta
       r = zeros(p_end,1);                    t = zeros(p_end,1);
for n = 1 : nH
    r(1) = sqrt(X1^2 + X2^2);              t(1) = pi-asin(X2/r(1));
     f_r = 0;     st_0 = X2;     % start far away (with f_r = f/r)
     eps = 1;                    % indicator of geodesic
   for p = 1 : p_end
     if r(p) > 1
     f_r = (3*pi/8-1) / r(p)^3;
    g_rr = 1/(1-2*f_r)^2;                  g_tt = (r(p)/(1+f_r))^2;
    sr_p = sqrt(abs(1-st_0^2/g_tt)/g_rr);  st_p = st_0/g_tt;
   else
     n_S = sqrt(2-r(p)^2);                      % Luneberg lens
     f_r = (6*asin(r(p)/sqrt(2))-3*n_S*r(p)*(n_S^2-1))/(4*r(p)^3)-1;
    g_rr = 1/(1+3*(n_S-1)-2*f_r)^2;        g_tt = r(p)^2/(1+f_r)^2;
    sr_p = sqrt(abs(1-st_0^2/g_tt)/g_rr);  st_p = st_0/g_tt;
   end
   if (1-st_0^2/g_tt)< 0; eps= -1; end          % at the perihelion
      dr = sr_p * ds;                       dt = st_p * ds;
  r(p+1) = r(p) - eps * dr;              t(p+1) = t(p) - dt;
  end % p-loop
     x1n = r .* cos(t);                    x2n = r .* sin(t);
   plot(x1n, x2n,'-k','LineWidth',1);          % plot geodesics
      X2 = X2 - dH;                            % change start
end % n_loop
```

Figure 9. Matlab script to construct and plot the geodesics for the Lüneberg lens, using piecewise linear approximation.

5. *Emergent behavior inside inhomogeneous media.*

Growing interest in spin-wave dynamics, see Mahmoud et al. (2020) and Prabhakar and Stancil (2009), has led to the use of graded-index lenses for steering magnetostatic excitations. In quantum computing design, one aims to guide such waves using graded-index lenses. Although such lenses are typically designed for light, the same analysis applies when the refractive index is replaced by magnetic susceptibility. Whitehead et al. (2018) used ray theory to replicate Lüneburg-lens focusing of spin waves, and later Whitehead et al. (2019) examined steering within an Eaton lens characterized by the index profile $n_S = \sqrt{2r_S/r - 1}$. The singularity at $r = 0$ was interpreted as enabling 180° steering. Ray theory, however, does not account for the emergent behavior of material points adjacent to the rays. Our model provides a weak-field spatial formulation in which the refractive tension follows from an integration of the refractive index throughout the lens interior and exterior, see (Equation 45). For the Eaton lens the integral admits an analytical expression and substituting f/r into our minimal numerical

implementation, see Figure 9, shows that ray-based approximations are unnecessary: the emergent wave behavior is naturally and fully captured by the geodesic-based model.

9. Conclusions

In this work, we have presented a generalized theoretical framework for describing the propagation of electromagnetic radiation in inhomogeneous media by reformulating the problem in terms of geodesic motion within an effective optical geometry. Starting from the conventional geometrical optics approximation, where light propagates along rays and the optical length is defined by the line element scaled by the speed of light in vacuum, we extended this description by introducing a geometrical tensor that depends explicitly on the local refractive index. This approach allowed us to redefine electromagnetic propagation as following geodesics in a Riemannian space, rather than classical rays in Euclidean space. By altering the local frame of reference, we demonstrated that the optical length remains invariant, highlighting the geometrical nature of the propagation mechanism. The introduction of a refractive-index-dependent geometry results in a curved optical space, even in the absence of gravitational fields, offering a new perspective on wave behavior near refractive structures. We showed that the influence of objects with constant refractive index embedded in vacuum extends beyond their physical boundaries, producing measurable effects in the surrounding medium. This emergent property, not accounted for in classical ray optics, stems from the global nature of the wave propagation along geodesics and represents a fundamental shift in how we interpret the interaction of waves with inhomogeneous media. A key result of our analysis is the interpretation of electromagnetic energy along the geodesic as the difference between kinetic and potential energy, leading to an evolution equation for the intensity that is governed by the local group velocity. This group velocity encapsulates the local deformation of the optical geometry and can be understood as a manifestation of spatial dispersion, whereas the phase velocity remains equal to the vacuum speed of light due to the constancy of the phase front propagation. To validate our framework, we applied it to the case of a homogeneous spherical object with varying refractive index, computing both the geodesic trajectories and the propagation of harmonic waves along them. The results revealed distinctive features not predicted by ray-based models, especially in the transition zones near the object's boundary.

Two practical applications illustrated the utility of the theory. First, in the context of astrophysical measurements, we calculated the two-way Shapiro time delay for a satellite approaching the Sun, incorporating the effect of the solar corona's refractive properties. Second, we analyzed the focusing behavior of a Lüneburg lens, comparing classical ray predictions with the geodetic analysis. The latter captured additional wave effects and provided a more comprehensive description of the focusing mechanism.

In summary, the geodesic-based formulation of electromagnetic propagation offers a powerful extension to traditional ray optics. It provides a unified geometric interpretation of wave behavior in both near-field and far-field regimes. It accounts for effects neglected in classical treatments and offers direct connections to established electromagnetic theory. The framework has broad applicability across disciplines, including interstellar communication, astrophysical diagnostics, and advanced lens design, particularly in systems involving broadband or nontrivial refractive profiles. It enables deeper insights into the interplay between geometry, spatial dispersion, and wave dynamics.

Conflict of Interest

The authors declare no conflicts of interest relevant to this study.

Data Availability Statement

All numerical results can be reproduced by using the data and information available in the listed references and figures included in this paper.

Acknowledgments
The authors thank the reviewers for their positive and constructive comments, and Dr. R. F. Remis for the stimulating discussions that contributed to improving this paper.

References

Abubakar, A., & Van den Berg, P. M. (2004). Iterative forward and inverse algorithms based on domain integral equations for three-dimensional electric and magnetic objects. *Journal of Computational Physics*, *195*(1), 236–262. https://doi.org/10.1016/j.jcp.2003.10.009

Benningfield, D. (2020). A better understanding of how the Sun bends light, source: Radio science. *Eos*, *101*, 236–262. https://doi.org/10.1029/2019EO150599

Born, M. A., & Wolf, E. (1959). *Principles of optics*. Pergamon Press.

Chyla, W. T. (2012). Simultaneous gravitational and refractive lensing. *International Journal of Astronomy and Astrophysics*, *2*(2), 76–80. https://doi.org/10.4236/ijaa.2012.22011

de Souza Sánchez Filho, E. (2015). *Tensor calculus for engineers and physicists*. Springer.

Dietrich, O. (2016). Symmetric 3×3 matrices with repeated eigenvalues. https://doi.org/10.13140/RG.2.1.1156.8240

Fokkema, J. T., & Van den Berg, P. M. (2019). Additional bending of light in Sun's vicinity by its interior index of refraction. *arXiv preprint arXiv:1806.05045*. https://doi.org/10.48550/arXiv.1806.05045

Fokkema, J. T., & Van den Berg, P. M. (2020). On the propagation paths and wavefronts in the vicinity of a refractive object. *Radio Science*, *55*, 1–15. https://doi.org/10.1029/019RS007021

Gómez, J. E., Padilla-Ortiz, A. L., Jaimes-Nájera, A., Trevino, J. P., & Chávez-Cerda, S. (2021). Generalization of ray tracing in symmetric gradient-index media by Fermat's ray invariants. *Optics Express*, *21*, 33010–33026.

Lüneburg, R. K. (1944). *Mathematical theory of optics. Providence*. Brown University Press.

Mahmoud, A., Ciubotaru, F., Chumak, F. V. A. V., Hamdioui, S., Adelman, C., & Cotofana, S. (2020). Introduction to spin wave computing. *Journal of Applied Physics*, *128*, 161101.

Misner, C. W., Thorne, K., & Wheeler, J. (2017). *Gravitation*. Princeton University Press.

Nazeri, B., & Nouri-Zonoz, M. (2011). Electromagnetic Casimir effect and the spacetime index of refraction. *arXiv preprint arXiv:1110.4257*. https://doi.org/10.1103/PhysRevD.85.044060

Prabhakar, A., & Stancil, D. D. (2009). *Spin waves, theory and applications*. Springer.

Sebástian, A., Acedo, L., & Morano, J. (2022). An orbital model for the Parker Solar Probe mission: Classical vs relativistic effects. *Science*.

Shapiro, I. I. (1964). Fourth test of general relativity. *Physical Review Letters*, *13*(26), 789–791. https://doi.org/10.1103/physrevlett.13.789

Shapiro, I. I., Ash, M. E., Ingalls, R. P., Smith, W. B., Campbell, D. B., Dyce, R. B., et al. (1971). Fourth test of general relativity: New radar result. *Physical Review Letters*, *26*(18), 1132–1135. https://doi.org/10.1103/physrevlett.26.1132

Shapiro, I. I., Pettingill, G. H., Ash, M. E., Stone, M. L., Smith, W. B., Ingalls, R. P., & Brockelman, R. A. (1968). Fourth test of general relativity: Preliminary results. *Physical Review Letters*, *20*, 1265–1269.

Shapiro, I. I., Reasenberg, R. D., MacNeil, P. E., Goldstein, R. B., Brenkle, J. P., Cain, D. L., et al. (1977). The viking relativity experiment. *Journal of Geophysical Research*, *82*(28), 4329–4334. https://doi.org/10.1029/js082i028p04329

Šilhavý, M. (1997). *The mechanics and thermodynamics of continuous media*. Springer.

Sokol, J. (2018). A place in the Sun. *Science*, *361*(6401), 441–445. https://doi.org/10.1126/science.361.6401.441

Synge, J. L., & Schild, A. (1978). *Tensor Calculus*. Dover.

Van den Berg, P. M. (2021). *Forward and inverse scattering algorithms based on contrast source integral equations*. Wiley.

Whitehead, N. J., Horsley, S. A. R., Philbin, T. G., & Kruglyak, V. V. (2018). A Luneburg lens for spin waves. *Applied Physics Letters*, *113*(21), 212404. https://doi.org/10.1063/1.5049470

Whitehead, N. J., Horsley, S. A. R., Philbin, T. G., & Kruglyak, V. V. (2019). Graded index lenses for spin wave steering. *Physical Review B: Condensed Matter*, *100*(9), 094404. https://doi.org/10.1103/physrevb.100.094404

Ye, X. H., & Lin, Q. (2007). Gravitational lensing analyzed by graded index of vacuum. *arXiv:0711.11.0633v2[gr-qc]*, *10*(7), 075001. https://doi.org/10.1088/1464-4258/10/7/075001

Yun, Y. H., & Jang, K. (2022). Light refraction and reflection near a black hole. *Journal of High Energy Physics, Graviation and Cosmology*, *8*(1), 228–236. https://doi.org/10.4236/jhepgc.2022.81016